

A Photon-Photon Quantum Gate Based on Rydberg Interactions

Daniel Tiarks, Steffen Schmidt-Eberle, Thomas Stolz, Gerhard Rempe, and Stephan Dürr
Max-Planck-Institut für Quantenoptik, Hans-Kopfermann-Str. 1, 85748 Garching, Germany

Different types of interactions in quantum systems are currently being investigated regarding their suitability for future quantum technologies. One promising candidate is the strong and long-range interaction between Rydberg states of neutral atoms, for which first applications in the fields of quantum computation [1] and quantum simulations [2–4] have been reported in recent years. Using electromagnetically induced transparency, these Rydberg interactions can be mapped to light [5–15], thus creating an effective interaction between photons. Here we extend the range of applicability of these interactions to the field of quantum communication and quantum networking [16] by realising a photon-photon quantum gate [17, 18]. To achieve this, a photonic control qubit is stored in a Rydberg quantum memory in an ultracold atomic gas. This qubit interacts with a propagating photonic target qubit coupled to a Rydberg state to generate a conditional π phase shift. Finally, the control photon is retrieved. We measure controlled-NOT truth tables with fidelities 0.66(9) and 0.70(8) and an entangling-gate fidelity of 0.637(45). The demonstration of a photon-photon quantum gate is the hallmark for having achieved full quantum control of one photon over another. The level of control achieved here is an important step on one hand for exploring novel many-body states of photons and on the other hand for applications in quantum communication and quantum networking. A prominent example is deterministic photonic Bell-state detection which is crucial for quantum repeaters.

Optical technologies serve as today’s standard for distributing information in the Internet since photons offer high speed and large bandwidth. Because of these benefits, future quantum technologies will probably rely on photonic qubits to transfer quantum states between distant nodes. However, ambitions to use photons for processing rather than only transmitting qubits are hampered by the fact that photons hardly interact with each other. A solution to this problem is offered by a Rydberg polariton [6–15]. This intriguing quasiparticle - composed of a photonic component and an atomic Rydberg excitation - is obtained when a photon enters a medium in which electromagnetically induced transparency (EIT) couples the photon to a Rydberg state. The key idea is that the atomic Rydberg components create a strong long-range interaction between two Rydberg polaritons. Many schemes for implementing a photon-photon gate based on Rydberg interactions have been

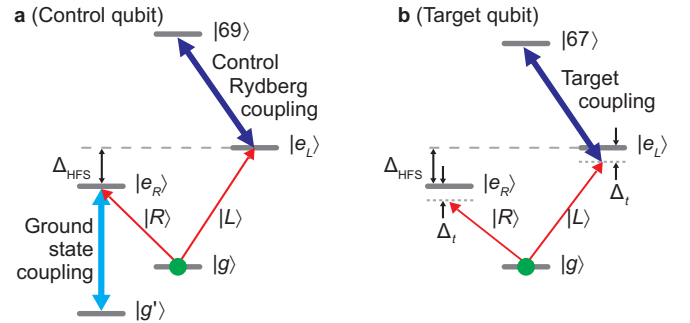


FIG. 1: Atomic level schemes. **a**, Level scheme for EIT storage of the control qubit. The initial population (green) is prepared in state $|g\rangle$. $|L\rangle$ polarisation is stored in a Rydberg state $|69\rangle$, $|R\rangle$ polarisation in a ground state $|g'\rangle$. **b**, Level scheme for the target qubit. $|L\rangle$ polarisation propagates as a Rydberg polariton involving Rydberg state $|67\rangle$, $|R\rangle$ polarisation propagates off resonantly without experiencing EIT.

proposed [6, 7, 19–26] but the experimental realisation is still an important open goal.

The photon-photon quantum gate demonstrated here relies on a conditional π phase shift arising from the interaction between a stored excitation and a propagating Rydberg polariton. The quantum memory used for storage is characterised by an average fidelity $F_m = 0.875(7)$. In our experiment, the conditional π phase shift is accumulated from the direct interaction of the two wave packets during their spatiotemporal overlap. This is a long-standing goal since the 1980s, where it was the basis for the first proposal for a quantum gate for photons [27]. Previous experimental realisations of photon-photon quantum gates circumvented the difficulty in achieving a direct interaction. As a workaround, they relied either on linear optics combined with inherently probabilistic protocols [17] or on a sequence of two atom-photon gates [18].

The experiment begins with the preparation of a gas of $\sim 10^5$ ultracold ^{87}Rb atoms in an optical dipole trap at a temperature of typically $0.5 \mu\text{K}$ (see Appendix). The internal state is prepared in the $|g\rangle = |5S_{1/2}, F = m_F = 2\rangle$ ground state, where F, m_F are the hyperfine quantum numbers. The incoming control photon at a wavelength of 780 nm is resonant with the transition to the $5P_{3/2}, F = 3$ state (Fig. 1a). The lefthanded circular polarisation state $|L\rangle$ of this photon is stored in the Rydberg state $|69\rangle = |69S_{1/2}, F = m_F = 2\rangle$ using resonant Rydberg EIT (see Appendix) with intermediate state $|e_L\rangle = |5P_{3/2}, F = m_F = 3\rangle$ and control Rydberg coupling light at 480 nm.

Additionally, we store the righthanded circular polaris-

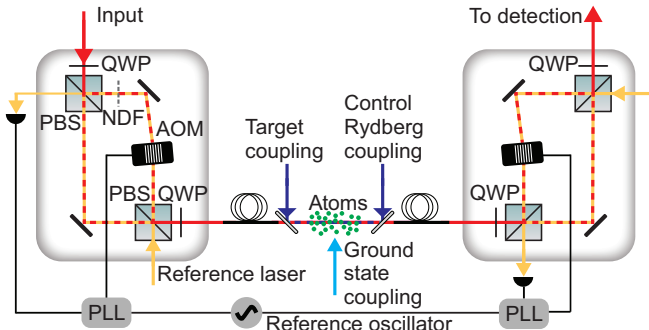


FIG. 2: Simplified scheme of the experimental setup. The control photon (red) passes through a first interferometer (left box), interacts with the atomic ensemble (green), and finally passes through a second interferometer (right box). The first interferometer shifts the frequency of only the $|R\rangle$ polarisation by $\Delta_{\text{HFS}}/2\pi$. The second interferometer removes this frequency shift. Counterpropagating reference light (yellow) and phase-locked loops (PLLs) stabilise each interferometer against thermal drift. Coupling light (blue, cyan) establishes EIT.

sation state $|R\rangle$ in the $|g'\rangle = |5S_{1/2}, F = m_F = 1\rangle$ ground state. This is not straightforward because the states $|g'\rangle$ and $|5P_{3/2}, F = 3\rangle$ are not connected by an electric-dipole transition because of $\Delta F = 2$. We overcome this hurdle by frequency shifting selectively only the $|R\rangle$ component of the control photon to make it resonant with the transition from $|g\rangle$ to $|e_R\rangle = |5P_{3/2}, F = 2, m_F = 1\rangle$. From here, we achieve resonant EIT-based storage in $|g'\rangle$ using ground-state coupling light at 780 nm. In addition, the frequency shift creates a large detuning from the Rydberg-EIT resonance, thus preventing undesired storage of the $|R\rangle$ polarisation in a Rydberg state. To create the required polarisation-dependent frequency shift of $\Delta_{\text{HFS}}/2\pi = 267$ MHz, we build a modified Mach-Zehnder interferometer using an acousto-optic modulator (AOM), polarising beam splitters (PBSs), and quarter-wave plates (QWPs) (left half of Fig. 2).

The storage is achieved by simultaneously switching off both control coupling light fields while the control photon is inside the medium. After a dark time set to 4.5 μs , both control coupling light fields are simultaneously switched back on and both polarisation components of the control qubit are retrieved. To remove the frequency shift of the $|R\rangle$ component, the retrieved light is sent through a similar interferometer (right half of Fig. 2). Overall, this realises an EIT-based quantum memory, which is sophisticated insofar as this memory stores one polarisation component in a Rydberg state and the other in a ground state. This has the decisive advantage that only the Rydberg component will strongly interact with the target photon when it propagates through the medium during the dark time, thus making a quantum gate possible. The average fidelity [28] of the quantum memory is $F_m = 0.875(7)$ (see Appendix), which clearly exceeds the classical limit 2/3.

To build a photon-photon gate, we combine this quantum memory for the control qubit with a conditional π phase shift generated by propagating the target photon through the medium during the dark time of the memory [13]. The $|L\rangle$ component of the target photon propagates as a Rydberg polariton, experiencing Rydberg EIT with intermediate state $|e_L\rangle$ (Fig. 1b) and with Rydberg state $|67\rangle = |67S_{1/2}, F = m_F = 2\rangle$, which features a Förster resonance with the $|69\rangle$ state [12]. The target photon pulse lasts 2.6 μs . The accompanying target coupling light at 480 nm is on for 4.1 μs to leave room for the $\sim 0.4 \mu\text{s}$ EIT group delay experienced by target state $|L\rangle$. The target state $|L\rangle$ is $\Delta_t/2\pi = -17$ MHz detuned (to the red) from the $|g\rangle \leftrightarrow |e_L\rangle$ resonance and propagation through the medium changes the target state $|L\rangle$ to $e^{-OD_L/2-i\beta_L}|L\rangle$ where OD_L is the optical depth and β_L the accumulated phase shift. In the presence of a stored $|L\rangle$ component of the control qubit, Rydberg blockade modifies the linear electric susceptibility χ experienced by the target qubit. This changes the optical depth and the phase shift to OD_{LL} and β_{LL} . The conditional optical depth is $\Delta OD = OD_{LL} - OD_L$ and the conditional phase shift $\Delta\beta = \beta_{LL} - \beta_L$.

Besides achieving $\Delta\beta = \pi$, a high-fidelity gate simultaneously requires $\Delta OD = 0$. Hence, for a given value of Δ_t , we carefully zero ΔOD by fine tuning the target two-photon detuning to be slightly off from the two-photon resonance (see Appendix). In addition, we carefully choose the combination of atom number and length of the medium to achieve $\Delta\beta = \pi$ and, for experimental convenience, $\beta_L - \beta_R = \pi$, where β_R is the phase shift experienced by an $|R\rangle$ polarised target photon, in the absence of a control photon. In contrast to Ref. [13], we operate at $\Delta OD = 0$ and at larger $|\Delta_t|$.

The control and target photons enter and leave the atomic ensemble at different times but have identical transverse mode and propagation direction. In particular, the target photon passes through both interferometers, just like the control photon. Hence, the target state $|R\rangle$ is 17 MHz red detuned from the $|g\rangle \leftrightarrow |e_R\rangle$ transition (Fig. 1b). This transition has a relatively small dipole matrix element, making its resonant optical depth a factor of 6 smaller than for the $|g\rangle \leftrightarrow |e_L\rangle$ transition. In addition, the target state $|R\rangle$ is $\Delta_{\text{HFS}}/2\pi$ red detuned from the two-photon resonance of Rydberg EIT, which means the target state $|R\rangle$ does not experience EIT. With these parameters, the target state $|R\rangle$ has fairly high transmission $e^{-OD_R} \sim 0.77$ (for count rates see Appendix), acquires some phase shift $\beta_R \sim 0.9$ rad, and the control qubit affects neither OD_R nor β_R . Lacking EIT, the target state $|R\rangle$ experiences negligible group delay, so that the longitudinal wave-packet overlap of the target states $|R\rangle$ and $|L\rangle$ deteriorates. Hence, in our data analysis of the transmitted target pulse, we include only those typically 2.0 μs in which the $|R\rangle$ and $|L\rangle$ components have good overlap. Each incoming qubit is implemented as an attenuated light pulse with Poissonian photon number statistics and mean photon number below unity. Data

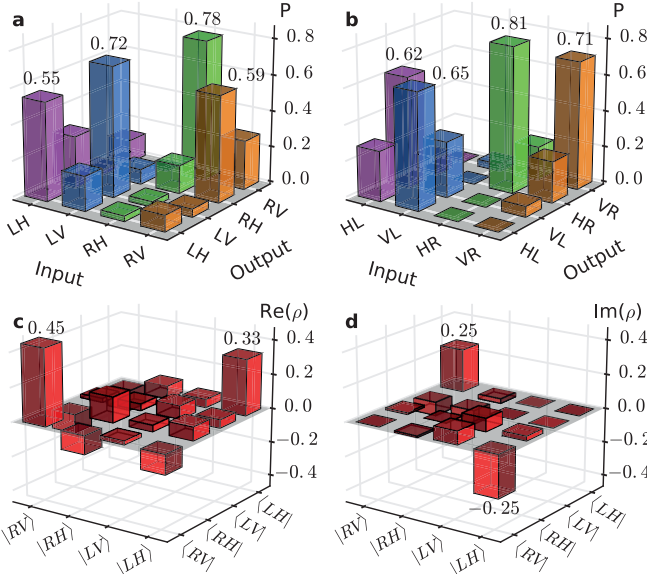


FIG. 3: Performance of the photon-photon gate. **a**, Truth table of the CNOT gate operation. To obtain a truth table, one of the four displayed input states is prepared repeatedly and the probability P to obtain the displayed output states is measured. Ideally, the target polarisations $|H\rangle$ and $|V\rangle$ should be exchanged if and only if the control qubit is in $|R\rangle$. **b**, Same as in part a but with the input polarisations of control and target swapped. **c**, Real and **d**, imaginary parts of the reconstructed density matrix ρ of the two-photon state created in the entangling-gate operation.

are postselected upon detection of one photon in each pulse to compensate for non-unity efficiencies and for the photon statistics of the input.

The polarisations $|R\rangle$ and $|L\rangle$ have different overall transmissions. For one qubit, this is easily compensated at the cost of reduced overall efficiency by placing an appropriate neutral density filter (NDF) into one arm of the first interferometer. As the ratio between the $|R\rangle$ and $|L\rangle$ transmissions is different for control and target qubit, we additionally temporally switch the radio-frequency (rf) power driving the AOM in the first interferometer to obtain the appropriate compensation for the other qubit.

Combination of the quantum memory with the conditional phase shift $\Delta\beta = \pi$ and the target-qubit phase shift $\beta_L - \beta_R = \pi$ should ideally yield a truth table $|RR\rangle \mapsto |RR\rangle$, $|RL\rangle \mapsto -|RL\rangle$, $|LR\rangle \mapsto |LR\rangle$, and $|LL\rangle \mapsto |LL\rangle$, where the control-qubit state is listed first. This constitutes a controlled phase flip gate, which is a universal two-qubit gate.

We now turn to the characterisation of this gate. Fig. 3a shows a measured CNOT truth table in which the target photon is initially in the horizontal $|H\rangle = (|R\rangle + |L\rangle)/\sqrt{2}$ or vertical $|V\rangle = i(|R\rangle - |L\rangle)/\sqrt{2}$ polarisation state, while the control photon is initially in $|R\rangle$ or $|L\rangle$. The fidelity of this truth table, i.e. the probability of obtaining the desired output averaged over all four input states, is $F_{\text{CNOT}} = 0.66(9)$. Fig. 3b shows a simi-

lar CNOT truth table but with the input polarisations of control and target swapped, yielding $F_{\text{CNOT}} = 0.70(8)$.

To demonstrate that the gate operates in the quantum regime, we study an entangling-gate operation. To this end, we prepare the input state $|HH\rangle$. From this, the gate should ideally produce the maximally-entangled output state $|\psi_i\rangle = (|LH\rangle - i|RV\rangle)/\sqrt{2}$. The actual output state can be described by a density matrix ρ . We measure a fidelity of $F_e = \langle \psi_i | \rho | \psi_i \rangle = 0.637(45)$ (linear unbiased estimator). This is well above the threshold of $1/2$ for demonstrating entanglement. Using quantum state tomography, we reconstruct the density matrix ρ (linear unbiased estimator) (Fig. 3c,d). We note that in a simple model (see Appendix), the non-unity visibilities of the control qubit and the target qubit already set an upper bound of $0.76(4)$ to F_e . We believe that future improvements, for example regarding laser phase noise, will make it possible to improve the fidelity considerably, but a detailed analysis of the physical origins of the infidelities is beyond the present scope.

In conclusion, we realised a photon-photon quantum gate relying on a conditional π phase shift created by a direct interaction between the overlapping wave packets. Besides the above-mentioned possibility to improve the fidelity, improvements in efficiency seem possible as well. For example, EIT storage and retrieval with an efficiency of 0.92 has been achieved recently [29]. Once fidelity and efficiency are improved, the present scheme could be extended to the generation of entangled states of several photonic qubits, simply by transmitting more than one target photon in the presence of the same stored gate photon. Additionally, the techniques used here might allow for miniaturisation and transfer to solid-states systems. For example, interactions between Rydberg excitons in a solid have been observed recently [30].

This work was supported by Deutsche Forschungsgemeinschaft through Nanosystems Initiative Munich.

Appendix A: Atomic Ensemble

The atomic gas is trapped in an optical dipole trap, similar to Ref. [13]. The radial trapping frequency is ~ 100 Hz and the atomic ensemble is cigar shaped with a Gaussian density profile in the radial direction with a root-mean-square (rms) radius of $\sigma_r = 12 \mu\text{m}$. The axial trapping potential is box like and the axial density profile (along the z axis) is to a good approximation homogeneous with a full width at half maximum (FWHM) cloud size of typically $60 \mu\text{m}$. No measures have been taken to control the static electric field at the position of the atoms. The atomic ensemble is located in a glass cell with the nearest glass surfaces at a distance of 15 mm from the atoms.

Some changes regarding the atomic ensemble were implemented compared to Ref. [13]. The plug beams now have an elliptically shaped spot with waists ($1/e^2$ radii of intensity) of $15 \mu\text{m}$ horizontally (along the z axis) and

43 μm vertically and are operated at a power of 0.3 W each. The centers of the plug beams are now separated by typically $\Delta z = 100 \mu\text{m}$. The magnetic field applied along the symmetry axis of the dipole trap to stabilise the orientation of the atomic spins now has a value of 14 μT .

Appendix B: Rydberg EIT

Rydberg EIT is created using the 780-nm signal beam (red in Fig. 2) together with Rydberg coupling light. One Rydberg coupling laser at 480 nm (blue in Fig. 2) counterpropagates the signal beam. It is used to store and retrieve the $|L\rangle$ polarisation of the control pulse. The other Rydberg coupling laser at 480 nm (also blue in Fig. 2) copropagates with the signal beam. It is used to create detuned Rydberg EIT for the $|L\rangle$ polarisation of the target pulse. Both Rydberg coupling beams are overlapped with and separated from the EIT signal beam using dichroic mirrors. The Rydberg coupling beams have powers of typically $P_{L,c} = 140 \text{ mW}$ and $P_{L,t} = 26 \text{ mW}$. Their waists of $w_{L,c} = 21 \mu\text{m}$ and $w_{L,t} = 12 \mu\text{m}$ are both large compared to the waist of the EIT signal beam of $w_s = 8 \mu\text{m}$ so that spatial inhomogeneities in the coupling intensities sampled by the signal light are no major concern. From these parameters, we estimate coupling Rabi frequencies of $\Omega_{L,c}/2\pi = 25 \text{ MHz}$ and $\Omega_{L,t}/2\pi = 20 \text{ MHz}$. The fit to the EIT data in Fig. 4 yields a coupling Rabi frequency of $\Omega_{L,t}/2\pi = 12.5(3) \text{ MHz}$ for the target light, in reasonable agreement with the above estimate, and a dephasing rate of $\gamma_{rg} = 1.2(3) \mu\text{s}^{-1}$, similar to the value obtained in Ref. [13].

As the EIT signal beam waist $w_s = 8 \mu\text{m}$ is much smaller than the Rydberg blockade radius of $R_B = 14 \mu\text{m}$ [13], the transverse degrees of freedom become irrelevant, suppressing fluctuations in ΔOD and $\Delta\beta$ otherwise caused by different relative transverse positions of the control and target photons. In addition, the medium is to a good approximation homogeneous in the longitudinal direction and the transverse size of the medium $\sigma_r = 12 \mu\text{m}$ is much larger than the $w_s = 8 \mu\text{m}$ EIT signal beam waist, which suppresses fluctuations in ΔOD and $\Delta\beta$ otherwise caused by storage of the control photon at positions with different atomic densities.

The differential group delay between the $|R\rangle$ and $|L\rangle$ polarisations of the target photon must be much shorter than the coherence time of the light source that creates the target photon. Otherwise, the coherence between the $|R\rangle$ and $|L\rangle$ polarisations would be reduced. In our experiment, the corresponding effect onto the visibility of the target qubit is negligible because the linewidth of the laser that creates the target photon is much smaller than the inverse group delay $\sim 1/(0.4 \mu\text{s}) = 2\pi \times 400 \text{ kHz}$. In addition, the narrow linewidths of this laser and of the target coupling laser help to reduce fluctuations in ΔOD and $\Delta\beta$, which are both sensitive to the two-photon detuning at the parameters where the experiment

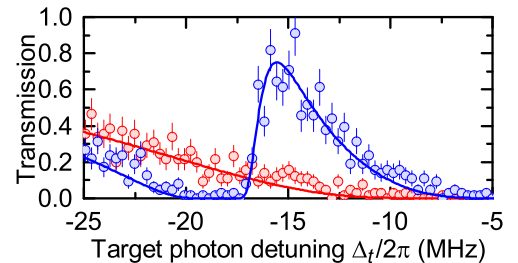


FIG. 4: Zeroing the conditional optical depth. The transmission of an $|L\rangle$ polarised target photon (blue) exhibits an EIT peak, with a maximum at the two-photon resonance at $\Delta_t/2\pi \sim -15 \text{ MHz}$. This feature is absent if the target coupling light is switched off (red). The lines show fits of the model from Ref. [13]. They cross at $\Delta_t/2\pi \sim -17 \text{ MHz}$. Here, the conditional optical depth ΔOD is approximately zero.

is performed.

Appendix C: Conditional Optical Depth

Zeroing the conditional optical depth ΔOD is important for a high-fidelity gate. Fine tuning the target detuning Δ_t based on data postselected upon detection of one control and one target photon would be quite time consuming. As an approximate but much faster method, we consider Fig. 4, which compares the target transmission with and without the target coupling laser, both recorded without sending a control photon into the system. Hence, no postselection upon a retrieved control photon is needed and the data acquisition rate is much higher. To understand, why Fig. 4 helps finding the two-photon detuning for which $\Delta OD = 0$, we consider the dependence of the first-order electric susceptibility $\chi(r)$ on the distance r between the propagating polariton and the stored excitation. Inspection of $\text{Im } \chi(r)$ for the parameters of our experiment shows that $\text{Im } \chi(r)$ is well approximated by a step function. For r larger than the blockade radius R_B we approximate $\text{Im } \chi(r)$ by $\text{Im } \chi(\infty)$. For $r \leq R_B$ we approximate $\text{Im } \chi(r)$ by $\text{Im } \chi(0)$. In Fig. 4, the blue and red data are measures for $\text{Im } \chi(\infty)$ and $\text{Im } \chi(0)$, respectively. Hence, $\Delta OD = 0$ is obtained for that value of Δ_t where the two lines in Fig. 4 cross. We use this approximate method to fine tune the value of Δ_t .

Appendix D: Quantum Memory

The 780-nm EIT signal light for the control and target pulses is split into two beams to individually manipulate polarisation, timing, and power of the control and target signal input pulses. The two beams are recombined on a non-polarising 50:50 beam splitter. Whenever we quote

the input polarisation of a photon, we refer to the polarisation at the point after this recombination, which is just before entering the first interferometer shown in Fig. 2.

The ground-state coupling light beam (cyan in Fig. 2) required to store and retrieve the $|R\rangle$ polarisation of the control photon propagates perpendicularly to the EIT signal light. It has a waist of $w_g = 64 \mu\text{m}$ and a power P_g between 0.8 and $1.6 \mu\text{W}$, which yields an estimated coupling Rabi frequency $\Omega_g/2\pi$ between 6 and 8 MHz.

To characterise the quantum memory, we perform single-photon polarisation tomography of the retrieved light. The normalised single-photon Stokes parameters are $S_i = (P_i - P_{i\perp})/(P_i + P_{i\perp})$, where $i \in \{H, D, R\}$ denotes horizontal, diagonal, and righthanded circular polarisation, P_i the power behind a polariser which transmits the polarisation i , and $H^\perp = V$, $D^\perp = A$, and $R^\perp = L$ denote vertical, anti-diagonal, and lefthanded circular polarisation. The visibility, i.e. the degree of (maximum) linear polarisation, is $V = (S_H^2 + S_D^2)^{1/2}$. The azimuth φ is defined modulo 2π by $S_H = V \cos \varphi$ and $S_D = V \sin \varphi$. For $S_R = 0$, V is a measure for how much coherence there is between the $|R\rangle$ and $|L\rangle$ polarisations. We denote the visibilities of the control and target qubits as V_c and V_t , respectively.

For an $|R\rangle$ polarised input, the retrieved light is found to have a fraction $\epsilon_R = 4.8(5)\%$ of its energy in $|L\rangle$. Likewise, for an $|L\rangle$ polarised input we obtain $\epsilon_L = 2.5(6)\%$ in $|R\rangle$. Hence, the two polarisations $|R\rangle$ and $|L\rangle$ are well maintained during storage. To test how well coherence between $|R\rangle$ and $|L\rangle$ is maintained, we choose an input superposition such that the $|R\rangle$ and $|L\rangle$ components of the output energy are fairly well balanced. The results of this measurement are shown in Fig. 5. Part a shows that the retrieved light powers in $|R\rangle$ and $|L\rangle$ are fairly well balanced at all relevant times. To minimise the influence of detector dark counts, we analyse data only in the unshaded region. Polarisation tomography yields the azimuth φ and the visibility V_c . These quantities, shown in parts b and c, are to a good approximation time independent, which is advantageous because it implies that we can effortlessly average data over the full data analysis time window. This averaging yields $V_c = 0.66(2)$. The average fidelity of the quantum memory is $F_m = (2 + 2V_c + (1 + \epsilon_R)^{-1} + (1 + \epsilon_L)^{-1})/6 = 0.875(7)$. For comparison, if light is sent through both interferometers in the absence of atoms, we measure $V = 0.97$ for an appropriate input state. Hence, V_c is predominantly limited by the atomic memory, not by the interferometers.

Various effects can limit the visibility V_c achievable in the control qubit after retrieval from the ground and Rydberg state. This is because the phase of the retrieved light depends on the relative phase accumulated during the dark time between an atomic superposition and a local oscillator, somewhat like in Ramsey spectroscopy. But in contrast to normal Ramsey spectroscopy, here three local oscillators instead of one contribute, namely the ground-state coupling laser at 780 nm, the control Rydberg coupling laser at 480 nm, and the rf reference

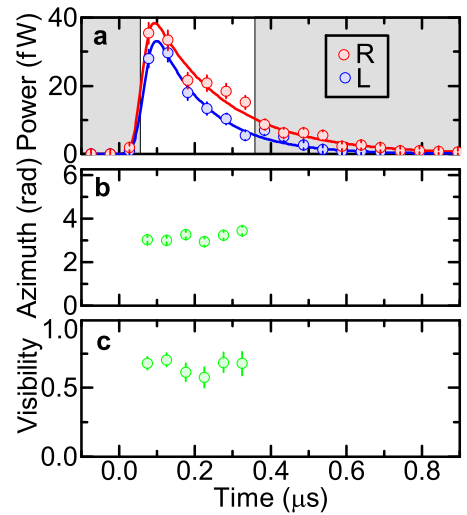


FIG. 5: Performance of the quantum memory for the control qubit. **a** The retrieved power is well balanced between $|R\rangle$ and $|L\rangle$ at all times. **b** Azimuth and **c** visibility of the retrieved light depend hardly on time. The visibility is high.

oscillator, which drives the PLLs in both interferometers. The large wavelength difference between these two lasers makes it difficult to achieve low relative phase noise between them. The very different principal quantum numbers of the atomic states result in large differential electric polarisabilities for static or dynamic electric fields. Overall, various effects contribute to phase fluctuations, e.g. phase fluctuations of both control coupling lasers, fluctuating Zeeman and Stark effects in the presence of fluctuating static magnetic and electric fields, fluctuating differential light shifts in the presence of power fluctuations in the dipole trapping light and in the target coupling light, and a distribution of differential light shifts in the dipole trapping light and in the target coupling light resulting from the thermal position distribution of the atoms. A preliminary analysis suggests that phase fluctuations of the control Rydberg coupling laser are the dominant limiting factor in the present setup.

Appendix E: Count Rates

The combined efficiencies for storage and retrieval of the control qubit for a dark time of $t_d = 4.5 \mu\text{s}$ in the presence of a target pulse are roughly $\eta_R \sim 0.1$ and $\eta_L \sim 0.03$ for the $|R\rangle$ and $|L\rangle$ polarisations, respectively. The transmission of an $|R\rangle$ polarised target qubit is $T_R = e^{-OD_R} \sim 0.77$. The transmission of an $|L\rangle$ polarised target qubit is roughly $T_L \sim 0.15$, in reasonable agreement with the transmission at the point, where the two lines in Fig. 4 cross. This yields an efficiency $\eta_j T_j$ between 0.005 and 0.08 for a photon pair to survive a gate operation, depending on the input polarisations $i, j \in \{R, L\}$. Note that future improvements regarding

these numbers are possible.

The EIT signal input light pulses are attenuated pulses created from a laser beam and have Poissonian photon number statistics. Typical values for the average photon numbers impinging onto the atomic ensemble are 0.33 and 0.50 for control and target pulse, respectively. Let P_{shot} denote the probability of a coincidence detection of one control and one target photon in a single experimental shot — consisting of storage of a control photon, propagation of a target photon, and retrieval of the control photon. In addition to the above-discussed efficiency $\eta_i T_j$ of the gate, several technical issues contribute to P_{shot} , namely non-unity transmissions through three optical fibres (two of them shown in Fig. 2 and another one right after the second interferometer), non-unity transmissions through both interferometers, and the quantum efficiency of 0.5 of each avalanche photodiode used for detection. In daily alignment, we typically measure $P_{\text{shot}} = 1.3 \times 10^{-5}$ for the entangling-gate operation. Such an experimental shot is repeated every 100 μs as in Ref. [13]. The illumination with light causes spontaneous emissions which result in loss of atoms by spontaneous evaporation from the shallow dipole trap. To avoid a noticeable drop in atom number, we perform only 10^4 experimental shots and then prepare a new atomic ensemble. A new atomic sample is prepared every 18 s so that in one minute, we detect an average number of 0.4 coincidences.

Appendix F: Modelling the Fidelity of the Entangling-Gate Operation

Fluctuations and nonideal average values in the experimental parameters reduce the fidelity of the entangling-gate operation. Here, we present a simple model of these effects, which yields an upper bound for the fidelity of the entangling-gate operation given the measured visibilities of the control qubit V_c and target qubit V_t . Of course, as soon as one manages to improve the visibilities, the upper bound will improve as well. For simplicity, we assume that nonideal behaviour comes entirely from fluctuations in the phases.

We assume that each realisation of the experiment yields an output state vector in which all of the states $|RR\rangle$, $|RL\rangle$, $|LR\rangle$, and $|LL\rangle$ have equal population. Hence, the output state vector has the general form

$$|\psi_\beta\rangle = \frac{1}{2}e^{-i\beta_0}(|RR\rangle + e^{-i\beta_2}|RL\rangle + e^{-i\beta_1}|LR\rangle + e^{-i\beta_1-i\beta_2-i\beta_3}|LL\rangle),$$

with four real phases β_0 , β_1 , β_2 , and β_3 . We identify $\beta_2 = \beta_L - \beta_R$ as the target-qubit phase shift and $\beta_3 = \Delta\beta$ as the conditional phase shift discussed above. We denote the phase shifts which storage and retrieval imprint onto the control qubit in the absence of a target qubit as $\beta_{c,L}$ and $\beta_{c,R}$. Hence $\beta_1 = \beta_{c,L} - \beta_{c,R}$ is the control-qubit phase shift, and $\beta_0 = \beta_R + \beta_{c,R}$ is a global phase. The

latter is irrelevant and we set $\beta_0 = 0$. The input state $|HH\rangle$ for the entangling-gate operation equals $|\psi_\beta\rangle$ with $\beta_1 = \beta_2 = \beta_3 = 0$. The ideal output state $|\psi_i\rangle$ equals $|\psi_\beta\rangle$ with $\beta_1 = 0$ and $\beta_2 = \beta_3 = \pi$. The state $|\psi_\beta\rangle$ has fidelity $F_\beta = |\langle\psi_i|\psi_\beta\rangle|^2 = [2 + \cos\beta_1 - \cos\beta_2 + \cos(\beta_1 + \beta_2 + \beta_3) - \cos(\beta_1 - \beta_2) - \cos(\beta_1 + \beta_3) + \cos(\beta_2 + \beta_3)]/8$ with the ideal state.

We use $\overline{\dots}$ to denote the average over the fluctuations of the phases β_1 , β_2 , and β_3 . Considering the control qubit in the absence of a target qubit, we obtain the output Stokes parameters $S_{H,\beta_1} = \cos\beta_1$, $S_{D,\beta_1} = \sin\beta_1$ and $S_{R,\beta_1} = 0$ for the input state vector $|H\rangle$ and a specific value of the random variable β_1 . The ensemble averages are $S_H = \overline{S_{H,\beta_1}} = \cos\beta_1$, $S_D = \overline{\sin\beta_1}$, and $S_R = 0$ so that the visibility is $V_c = V_1 = [(\sin\beta_1)^2 + (\cos\beta_1)^2]^{1/2}$. The fidelity between the single-qubit input state $|H\rangle$ and the single-qubit output state ρ_{out} is $F_1 = \langle H|\rho_{\text{out}}|H\rangle = (1 + S_H)/2$. The average value β_1 can be varied in the experiment. Assuming that V_1 remains unchanged when doing so, we obtain the maximum $F_{1,m} = \frac{1+V_1}{2}$. Likewise, considering only the target qubit in the absence of the control qubit, we obtain $V_2 = [(\sin\beta_2)^2 + (\cos\beta_2)^2]^{1/2}$ and $F_{2,m} = (1 + V_2)/2$. In analogy to these expressions, we formally define $V_3 = [(\sin\beta_3)^2 + (\cos\beta_3)^2]^{1/2}$ and $F_{3,m} = (1 + V_3)/2$.

We now turn to the entangling-gate operation. For the input state vector $|HH\rangle$, our model yields the output density matrix $\rho = |\psi_\beta\rangle\langle\psi_\beta|$ and the fidelity $F_e = \langle\psi_i|\rho|\psi_i\rangle = \overline{F_\beta}$. To evaluate this expression, we use trigonometric identities such as $\cos(\beta_1 + \beta_2) = \cos\beta_1 \cos\beta_2 - \sin\beta_1 \sin\beta_2$. For simplicity, we assume that the fluctuations in the variables β_1 , β_2 , and β_3 are uncorrelated. Hence, $\cos\beta_1 \cos\beta_2 = \overline{\cos\beta_1} \cos\beta_2$ etc. We assume that the average values $\overline{\beta_i}$ are chosen such that F_e is maximised at fixed values of V_1 , V_2 , and V_3 . We also assume that the probability distribution function of each β_i is symmetric around its average value. Hence, F_e is maximised if we choose $\overline{\beta_1} = 0$ and $\overline{\beta_2} = \overline{\beta_3} = \pi$. This yields $\sin\beta_i = 0$, $\cos\beta_1 = V_1$, $\cos\beta_2 = -V_2$, $\cos\beta_3 = -V_3$. A straightforward calculation now yields

$$F_e = \frac{1+V_1}{2} \frac{1+V_2}{2} \frac{1+V_3}{2} + \frac{1-V_3}{8}.$$

Using the same methods, we find that the visibility V_t measured in Ref. [13] in the presence of a stored $|L\rangle$ control excitation is $V_t = V_2 V_3$. Given the measured value V_t but with unknown V_2 and V_3 , the expression for F_e is maximised if we assume $V_2 = 1$ and $V_t = V_3$. As additional imperfections, such as events in which more than one control or more than one target photon impinge on the atomic sample, will tend to lower F_e even further, we obtain the upper bound $F_e \leq (1 + V_c)(1 + V_t)/4 + (1 - V_t)/8$. Using the value $V_c = 0.66(2)$ measured here and the value $V_t = 0.75(10)$ measured in Ref. [13], we obtain the upper bound $F_e \leq 0.76(4)$.

It is interesting to investigate whether the assumption that all imperfections are modeled as phase fluctuations has a large effect onto the resulting upper bound for F_e

at given measured values of V_c and V_t . To address this question, we developed an analogous model that is based purely on population fluctuations. As long as all fluctuations are small, we find that the resulting upper bound is identical to the upper bound estimated from pure phase fluctuations. In the experiment both types of fluctuations exist. But as the investigation of both extreme cases — pure phase fluctuations or pure population fluctuations — predict identical upper bounds, it seems likely that a model taking both types of fluctuations into account simultaneously will predict a similar upper bound, as long as all fluctuations are small.

Appendix G: Absence of Excitation Hopping

A recent experiment [15] observed excitation hopping between a propagating Rydberg polariton in the $|100S\rangle$

state and a stored Rydberg excitation in the $|99P\rangle$ state. In principle, an analogous process could occur in our experiment. But in practice, it is negligible for two reasons. First, both excitations in our experiment are in S states which makes hopping a much slower second-order process. Second, the states used in our experiment exhibit predominantly van der Waals interaction, not excitation hopping. To quantify this, the van der Waals interaction at distance r can be characterised by $V_b(r) = -C_6/r^6$ and the second-order excitation hopping by $V_{ex}(r) = -\chi_6/r^6$, see e.g. Ref. [15]. We use quantum defect theory to calculate $C_6/\chi_6 = 29$ for the states used in our experiment, which shows that van der Waals interaction dominates.

- [1] Saffman, M. Quantum computing with atomic qubits and Rydberg interactions: progress and challenges. *J. Phys. B* **49**, 202001 (2016).
- [2] Schauß, P. *et al.* Crystallization in Ising quantum magnets. *Science* **347**, 1455–1458 (2015).
- [3] Labuhn, H. *et al.* Tunable two-dimensional arrays of single Rydberg atoms for realizing quantum Ising models. *Nature* **534**, 667–670 (2016).
- [4] Bernien, H. *et al.* Probing many-body dynamics on a 51-atom quantum simulator. *Nature* **551**, 579–584 (2017).
- [5] Lukin, M. D. *et al.* Dipole blockade and quantum information processing in mesoscopic atomic ensembles. *Phys. Rev. Lett.* **87**, 037901 (2001).
- [6] Friedler, I., Petrosyan, D., Fleischhauer, M., & Kurizki, G. Long-range interactions and entanglement of slow single-photon pulses. *Phys. Rev. A* **72**, 043803 (2005).
- [7] Gorshkov, A. V., Otterbach, J., Fleischhauer, M., Pohl, T., & Lukin, M. D. Photon-photon interactions via Rydberg blockade. *Phys. Rev. Lett.* **107**, 133602 (2011).
- [8] Pritchard, J. D. *et al.* Cooperative atom-light interaction in a blockaded Rydberg ensemble. *Phys. Rev. Lett.* **105**, 193603 (2010).
- [9] Firstenberg, O. *et al.* Attractive photons in a quantum nonlinear medium. *Nature* **502**, 71–75 (2013).
- [10] Baur, S., Tiarks, D., Rempe, G., & Dürr, S. Single-photon switch based on Rydberg blockade. *Phys. Rev. Lett.* **112**, 073901 (2014).
- [11] Gorniaczyk, H., Tresp, C., Schmidt, J., Fedder, H., & Hofferberth, S. Single-photon transistor mediated by interstate Rydberg interactions. *Phys. Rev. Lett.* **113**, 053601 (2014).
- [12] Tiarks, D., Baur, S., Schneider, K., Dürr, S., & Rempe, G. Single-photon transistor using a Förster resonance. *Phys. Rev. Lett.* **113**, 053602 (2014).
- [13] Tiarks, D., Schmidt, S., Rempe, G., & Dürr, S. Optical π phase shift created with a single-photon pulse. *Sci. Adv.* **2**, 1600036 (2016).
- [14] Ningyuan, J. *et al.* Observation and characterization of cavity Rydberg polaritons. *Phys. Rev. A* **93**, 041802 (2016).
- [15] Thompson, J. D. *et al.* Symmetry-protected collisions between strongly interacting photons. *Nature* **542**, 206–209 (2017).
- [16] Kimble, H. J. The quantum internet. *Nature* **453**, 1023–1030 (2008).
- [17] O'Brien, J. L., Pryde, G. J., White, A. G., Ralph, T. C., & Branning, D. Demonstration of an all-optical quantum controlled-NOT gate. *Nature* **426**, 264–267 (2003).
- [18] Hacker, B., Welte, S., Rempe, G., & Ritter, S. A photon-photon quantum gate based on a single atom in an optical resonator. *Nature* **536**, 193–196 (2016).
- [19] He, B., Sharypov, A. V., Sheng, J., Simon, C., & Xiao, M. Two-photon dynamics in coherent Rydberg atomic ensemble. *Phys. Rev. Lett.* **112**, 133606 (2014).
- [20] Paredes-Barato, D. & Adams, C. S. All-optical quantum information processing using Rydberg gates. *Phys. Rev. Lett.* **112**, 040501 (2014).
- [21] Khazali, M., Heshami, K., & Simon, C. Photon-photon gate via the interaction between two collective Rydberg excitations. *Phys. Rev. A* **91**, 030301 (2015).
- [22] Hao, Y. M. *et al.* Quantum controlled-phase-flip gate between a flying optical photon and a Rydberg atomic ensemble. *Sci. Rep.* **5**, 10005 (2015).
- [23] Das, S. *et al.* Photonic controlled-PHASE gates through Rydberg blockade in optical cavities. *Phys. Rev. A* **93**, 040303 (2016).
- [24] Wade, A. C. J., Mattioli, M. & Mølmer, K. Single-atom single-photon coupling facilitated by atomic-ensemble dark-state mechanisms. *Phys. Rev. A* **94**, 053830 (2016).
- [25] Murray, C. R. & Pohl, T. Coherent photon manipulation in interacting atomic ensembles. *Phys. Rev. X* **7**, 031007 (2017).
- [26] Lahad, O. & Firstenberg, O. Induced cavities for photonic quantum gates. *Phys. Rev. Lett.* **119**, 113601 (2017).
- [27] Milburn, G. J. Quantum optical Fredkin gate. *Phys. Rev. Lett.* **62**, 2124–2127 (1989).
- [28] Bowdrey, M. D., Oi, D. K. L., Short, A. J., Banaszek,

K., & Jones, J. A. Fidelity of single qubit maps. *Phys. Lett. A* **294**, 258–260 (2002).

[29] Hsiao, Y.-F. *et al.* Highly efficient coherent optical memory based on electromagnetically induced transparency. *Phys. Rev. Lett.* **120**, 183602 (2018).

[30] Kazimierczuk, T., Fröhlich, D., Scheel, S., Stolz, H., & Bayer, M. Giant Rydberg excitons in the copper oxide Cu₂O. *Nature* **514**, 343–347 (2014).